Eur. Phys. J. A **19**, 221–229 (2004)
DOI 10.1140/epja/i2003-10101-8

THE EUROPEAN PHYSICAL JOURNAL A

# Effect of density-dependent nucleon-nucleon cross-section on elastic scattering

A.Sh. Ghazal[1,a], M.S.M. Nour El-Din[2], and M.Y.M. Hassan[1]

[1] Physics Department, Faculty of Science, Cairo University, Giza, Egypt
[2] Physics Department, Faculty of Science, Zagazig University (Benha Branch), Benha, Egypt

Received: 11 February 2003 / Revised version: 8 July 2003 /
Published online: 26 January 2004 – 
Communicated by A. Molinari

**Abstract.** A linear form of density-dependent total nucleon-nucleon (NN) cross-section that depends on the coordinates of the projectile and target is applied in the Glauber phase shift formula. The only free parameter in these calculations is the density-dependent parameter "$\beta$", which is adjusted to obtain an agreement between the calculated angular distribution of the elastic-scattering cross-section and the corresponding experimental one. The elastic scattering of the $^{12}$C ion on the $^{12}$C ion target has been studied at incident energies of 300, 360, 1016, 1441 and 2400 MeV. The total reaction cross-section "$\sigma_{\rm r}$" is also calculated with the obtained value of "$\beta$" for the same reactions. The obtained values of "$\sigma_{\rm r}$" are compared with those obtained from the optical-model analysis as well as those of the experimental value. Nuclear transparency effects are also discussed. Generally, the density-dependent NN cross-section improves the calculated results.

**PACS.** 24.10.-i Nuclear-reaction models and methods – 25.70.-z Low and intermediate energy heavy-ion reactions

## 1 Introduction

The study of elastic scattering is a basic ingredient to understand more complicated heavy-ion reactions. In the high-energy domain one of the models used for the analysis of elastic-scattering data is the microscopic Glauber model [1] based on the individual nucleon-nucleon collisions in the overlap volume of the colliding nuclei. Many attempts have been made to describe elastic-scattering processes between heavy ions in terms of the so-called optical limit to the Glauber model [2–8]. In the simple Glauber approach to heavy-ion elastic scattering, it is assumed that the flux attenuation of the elastic channel occurs by means of the classical straight-line trajectory. The scope of the Glauber model was extended to lower energies to study the differential elastic-scattering cross-section. This had been done by modifying the Glauber model to account for the Coulomb distortion of the trajectory occurring in case of heavy-ion scattering [4–6], the so-called modified Glauber model I. In the modified Glauber model I , the overlap integral of nuclear densities has been calculated along a trajectory characterized by the distance of closest approach.

The Coulomb modified Glauber model is developed to explain the new phenomena of the reaction cross-section ($\sigma_{\rm r}$) by considering the relation between the surface diffuseness of the neutron distribution and the neutron separation energy of the nuclei [9]. In this model, the free-space nucleon-nucleon cross-section $\sigma_{\rm NN}^{\rm free}$ obtained by experimental measurements is used. But, because of the effects of Pauli blocking and finite nuclear matter density in heavy-ion reactions, the real in-medium nucleon-nucleon cross-section $\sigma_{\rm NN}^{\rm in\text{-}medium}$ is different from the free nucleon-nucleon cross-section. As a result of Pauli suppression in the intermediate states, the in-medium nucleon-nucleon cross-section should have some density dependence and becomes smaller than in free space, especially in the low- and intermediate-energy regions [10]. The Pauli-blocking and Fermi-motion effects have been introduced via the local density approximation [11].

Many groups [12–15] have studied the medium effect of the nucleon-nucleon cross-section. As an attempt, Cai Xiangzhou *et al.* [16] proposed a new phenomenological formula for the in-medium NN cross-section. Ghazal [17], using the formula suggested by Cai Xiangzhou, studied the effect of the in-medium NN cross-section on the elastic scattering of heavy-ion reactions. Also, using this formula, Nour El-Din [18] calculated the total-reaction nucleus-nucleus cross-section according to Charagi approach [6],

[a] e-mail: ashgha@lycos.com

and no good agreement has been found for some reactions. The role of nuclear surface in the formation of the total-reaction cross-section is investigated by Lukyanov *et al.* [19]. Other approaches are introduced to take into account the in-medium effect [20]. A Taylor expansion of the in-medium cross-section in the density variable is introduced by Kalkow *et al.* [14]. A more recent approach, by Bertulani [21], obtained the lowest-order correction of the density dependence of in-medium NN cross-section from geometrical considerations of the Pauli-blocking effects.

In the present work, a microscopic approach that starts from the optical limit of the Glauber scattering theory and incorporates an approximate treatment of Pauli-blocking and Fermi-motion effects is introduced. It consists in replacing the total NN cross-section by a linear form (similar to that of Kalkow [14]) of the density-dependent NN cross-section that depends on the coordinates of the projectile and target through the exact position of the two interacting nuclei inside an integral defining the overlap densities of the colliding nuclei. These calculations allow one to describe the cross-section in terms of an elementary NN scattering process occurring inside the overlap of the densities of the colliding nuclei. In such a model, the only ingredients are the NN amplitude at 0° and the nuclear density. The formalism is introduced in sect. 2. Section 3 is devoted to the discussion of the obtained results.

## 2 Formalism

The nucleus-nucleus differential cross-section is given by

$$\frac{\mathrm{d}\sigma}{\mathrm{d}\Omega} \;=\; |f(\theta)|^2\,, \tag{1}$$

for different spinless nuclei, or

$$\frac{\mathrm{d}\sigma}{\mathrm{d}\Omega} \;=\; |f(\theta)+f(\pi-\theta)|^2\,, \tag{2}$$

for identical spinless nuclei, with the usual expression for the scattering amplitude $f(\theta)$ for charged particles:

$$f(\theta) = f_{\mathrm{c}}(\theta) \;+\; \frac{1}{2ik}\sum_{l=0}^{\infty}(2l+1) \times \exp(2i\sigma_l)\,(S_l-1)\,P_l(\cos\theta)\,, \tag{3}$$

where $k$ is the wave number, $f_{\mathrm{c}}(\theta)$ is the usual Coulomb scattering amplitude [22], $\sigma_l$ is the Coulomb phase shift and

$$S_l \;=\; \exp(2i\delta_l) \tag{4}$$

is the scattering matrix. In terms of the so-called optical limit to the Glauber model [2,14] the nuclear phase shift $\delta_l$ is written in the form

$$\delta_l = \;\frac{\pi}{k_{\mathrm{NN}}}\,\Omega_l\,f_{\mathrm{NN}}(0)\,, \tag{5}$$

where $k_{\mathrm{NN}}$ is the NN wave number and $\Omega_l$ is the overlap integral of the nuclear densities along the straight line characterized by the impact parameter $b = \frac{(l+1/2)}{k}$ and is given by [23]

$$\Omega(b) = \int \mathrm{d}^2b_{\mathrm{P}} \int_{-\infty}^{\infty} \mathrm{d}z_{\mathrm{P}} \int \mathrm{d}^2b_{\mathrm{T}} \int_{-\infty}^{\infty} \mathrm{d}z_{\mathrm{T}} \times\rho_{\mathrm{P}}(\vec{b}_{\mathrm{P}},z_{\mathrm{P}})\rho_{\mathrm{T}}(\vec{b}_{\mathrm{T}},z_{\mathrm{T}})f(\vec{b}_{\mathrm{T}}-(\vec{b}-\vec{b}_{\mathrm{P}}))\,, \tag{6}$$

where $\rho_i(r)$ is assumed to be of a Gaussian shape for the nuclear-matter density distribution for both the target and the projectile,

$$\rho_i(r_i) = \;\rho_i(0)\exp\left[-\frac{b_i^2+z_i^2}{a_i^2}\right], \tag{7}$$

where $i$ stands for P, T (projectile and target). The nuclear density parameters for $^{12}$C, $\rho_i(0)$ and $a_i$ are taken from Chauvin *et al.* [2] as well as from Charagi *et al.* [6] and are listed in table 1. The density parameters according to Chauvin *et al.* [2] (Chauvin's parameters) are based on the r.m.s. radius of $^{12}$C (2.37 fm) from electron scattering data [24], while those of Charagi *et al.* [6] (Charagi's parameters) are based on the adjustment of the experimentally determined surface texture (by matching the Gaussian profile with the profile calculated using the two-parameters Fermi distribution in the surface).

**Table 1.** The nuclear density parameters of $^{12}$C according to Chauvin *et al.* [2] and Charagi *et al.* [6].

| $^{12}$C | $\rho_i(0)$ (fm$^{-3}$) | $a_i$ (fm) |
|---|---|---|
| Chauvin [2] | 0.2974 | 1.935 |
| Charagi [6] | 0.3540 | 1.863 |

For the nucleon-nucleon range function $f(b)$, we also use the Gaussian form [23]:

$$f(b) \;=\; \frac{1}{\pi r_0^2}\exp\Big(-b^2/r_0^2\Big)\,, \tag{8}$$

where $r_0$ is the range parameter related to the slope of the nucleon-nucleon differential cross-section. The NN scattering amplitude ($f_{\mathrm{NN}}(0°)$) at $\theta = 0°$ is given by

$$f_{\mathrm{NN}}(0) \;=\; \frac{1}{4\pi}\,k_{\mathrm{NN}}\bar{\sigma}_{\mathrm{NN}}(\alpha_{\mathrm{NN}}+i)\,, \tag{9}$$

and the average NN cross-section $\bar{\sigma}_{\mathrm{NN}}$, averaged over neutron and proton numbers, is given by [6]

$$\bar{\sigma}_{\mathrm{NN}}(E) = \frac{N_{\mathrm{P}}N_{\mathrm{T}}\sigma_{\mathrm{nn}} + Z_{\mathrm{P}}Z_{\mathrm{T}}\sigma_{\mathrm{pp}} + (N_{\mathrm{P}}Z_{\mathrm{T}}+N_{\mathrm{T}}Z_{\mathrm{P}})\sigma_{\mathrm{np}}}{A_{\mathrm{P}}A_{\mathrm{T}}}, \tag{10}$$

where $A_{\mathrm{P}}$, $A_{\mathrm{T}}$, $Z_{\mathrm{P}}$, $Z_{\mathrm{T}}$, $N_{\mathrm{P}}$ and $N_{\mathrm{T}}$ are the projectile and target masses, charges and neutron numbers, respectively.

In view of eqs. (5)-(10), the nuclear phase shift $\delta_l$ can be written as

$$\delta(b) = \frac{\bar{\sigma}_{\rm NN}}{4}(\alpha_{\rm NN}+i)\int \mathrm{d}^2b_{\rm P}\int_{-\infty}^{\infty}\mathrm{d}z_{\rm P}\int \mathrm{d}^2b_{\rm T} \times\int_{-\infty}^{\infty}\mathrm{d}z_{\rm T}\rho_{\rm P}(\vec{b}_{\rm P},z_{\rm P})\rho_{\rm T}(\vec{b}_{\rm T},z_{\rm T})f(\vec{b}_{\rm T}-(\vec{b}-\vec{b}_{\rm P}))\,. \quad (11)$$

In our approach, we replace $\bar{\sigma}_{\rm NN}$ in eq. (11) by the following linear density-dependent form of the NN total cross-section:

$$\bar{\sigma}_{\rm NN}[1-\beta(\rho_{\rm P}(\vec{b}p,z_{\rm P})+\rho_{\rm T}(\vec{b}_{\rm T},z_{\rm T}))]\,. \quad (12)$$

A similar form is introduced in the calculation of the folding model optical potential when using a density-dependent effective NN interaction [17]. In this case eq. (11) can be written as

$$\delta(b) = \delta_0(b) - \beta[\delta_1(b)+\delta_2(b)]\,, \quad (13)$$

where

$$\delta_0(b) = \frac{\bar{\sigma}_{\rm NN}}{4}(\alpha_{\rm NN}+i)\int \mathrm{d}^2b_{\rm P}\int_{-\infty}^{\infty}\mathrm{d}z_{\rm P}\int \mathrm{d}^2b_{\rm T} \times\int_{-\infty}^{\infty}\mathrm{d}z_{\rm T}\rho_{\rm P}(\vec{b}_{\rm P},z_{\rm P})\rho_{\rm T}(\vec{b}_{\rm T},z_{\rm T})f(\vec{b}_{\rm T}-(\vec{b}-\vec{b}_{\rm P}))\,, \quad (14)$$

$$\delta_1(b) = \frac{\bar{\sigma}_{\rm NN}}{4}(\alpha_{\rm NN}+i)\int \mathrm{d}^2b_{\rm P}\int_{-\infty}^{\infty}\mathrm{d}z_{\rm P}\int \mathrm{d}^2b_{\rm T} \times\int_{-\infty}^{\infty}\mathrm{d}z_{\rm T}\rho^2_{\rm P}(\vec{b}_{\rm P},z_{\rm P})\rho_{\rm T}(\vec{b}_{\rm T},z_{\rm T})f(\vec{b}_{\rm T}-(\vec{b}-\vec{b}_{\rm P}))\,, \quad (15)$$

and

$$\delta_2(b) = \frac{\bar{\sigma}_{\rm NN}}{4}(\alpha_{\rm NN}+i)\int \mathrm{d}^2b_{\rm P}\int_{-\infty}^{\infty}\mathrm{d}z_{\rm P}\int \mathrm{d}^2b_{\rm T} \times\int_{-\infty}^{\infty}\mathrm{d}z_{\rm T}\rho_{\rm P}(\vec{b}_{\rm P},z_{\rm P})\rho^2_{\rm T}(\vec{b}_{\rm T},z_{\rm T})f(\vec{b}_{\rm T}-(\vec{b}-\vec{b}_{\rm P}))\,. \quad (16)$$

Performing these integrations over $b_{\rm P}$, $z_{\rm P}$ and $b_{\rm T}$, $z_{\rm T}$ using (7) and (8), one gets

$$\delta_0(b) = \frac{\bar{\sigma}_{\rm NN}\rho_{\rm P}(0)\rho_{\rm T}(0)a^3_{\rm P}a^3_{\rm T}\pi^2}{40(a^2_{\rm P}+a^2_{\rm T}+r^2_0)} \times(\alpha_{\rm NN}+i)\exp\left[-b^2/(a^2_{\rm P}+a^2_{\rm T}+r^2_0)\right]\,, \quad (17)$$

$$\delta_1(b) = \frac{\bar{\sigma}_{\rm NN}\rho^2_{\rm P}(0)\rho_{\rm T}(0)a^3_{\rm P}a^3_{\rm T}\pi^2}{40(a^2_{\rm P}+2a^2_{\rm T}+r^2_0)\sqrt{2}} \times(\alpha_{\rm NN}+i)\exp\left[-2b^2/(a^2_{\rm P}+2a^2_{\rm T}+r^2_0)\right]\,, \quad (18)$$

and

$$\delta_2(b) = \frac{\bar{\sigma}_{\rm NN}\rho_{\rm P}(0)\rho^2_{\rm T}(0)a^3_{\rm P}a^3_{\rm T}\pi^2}{40(2a^2_{\rm P}+a^2_{\rm T}+r^2_0)\sqrt{2}} \times(\alpha_{\rm NN}+i)\exp\left[-2b^2/(2a^2_{\rm P}+a^2_{\rm T}+r^2_0)\right]\,. \quad (19)$$

Assuming the deviation of the projectile trajectories due to the Coulomb field, the overlap integral of the nuclear densities is evaluated in terms of the distance of closest approach $b'(D)$ given by

$$D = b' \;=\; \frac{1}{k}\left[\eta+\left(\eta^2+b^2k^2\right)^{\frac{1}{2}}\right]\,, \quad (20)$$

instead of the impact parameter $b$, as suggested in refs. [4, 7,22]. $\eta$ is the Sommerfeld parameter given by

$$\eta = Z_1Z_2e^2/\hbar v\,, \quad (21)$$

where $v$ is the relative velocity between the target and the projectile.

In the framework of Glauber theory, the nucleus-nucleus reaction cross-section can be written as [6]

$$\sigma_{\rm r}(mb) = 20\pi\int b\mathrm{d}b[1-\exp(-\chi(b))]\,, \quad (22)$$

where

$$\chi(b) = 4\,\mathrm{Im}\,\delta(b)\,, \quad (23)$$

and "$\mathrm{Im}\,\delta(b)$" is the imaginary part of the nuclear phase shift given by eq. (13).

## 3 Results and discussion

The elastic scattering of $^{12}$C-$^{12}$C is studied at incident energies of 300, 360, 1016, 1441 and 2400 MeV. Calculations have been done in the framework of the optical limit of the Glauber scattering theory. A microscopic approach, that incorporates the density-dependent NN cross-section by a linear form that depends on the coordinates of the projectile and the target nuclei as an approximate treatment of the Pauli-blocking and Fermi-motion effects (eq. (12)), is used. The nuclear density of $^{12}$C is taken to be of Gaussian form given by eq. (7). The density parameters are listed in table 1. Using Chauvin's parameters, it is found that the calculated angular distribution of the elastic-scattering cross-section is better than that using Charagi's parameters in comparison with the experimental data. This could be seen in fig. 1. So we perform our calculations using Chauvin's density parameters. The calculations adopt the classical Coulomb trajectory given by eq. (20).

Figures 2-11 show the ratio of the calculated angular distribution to the Rutherford theoretical cross-sections ($\sigma/\sigma_{\rm R}$) displayed as a function of the C.M. scattering angle. In these figures, calculations have been done for both the density-independent ($\beta = 0$) and density-dependent ($\beta \neq 0$) total NN cross-section. The density-dependent

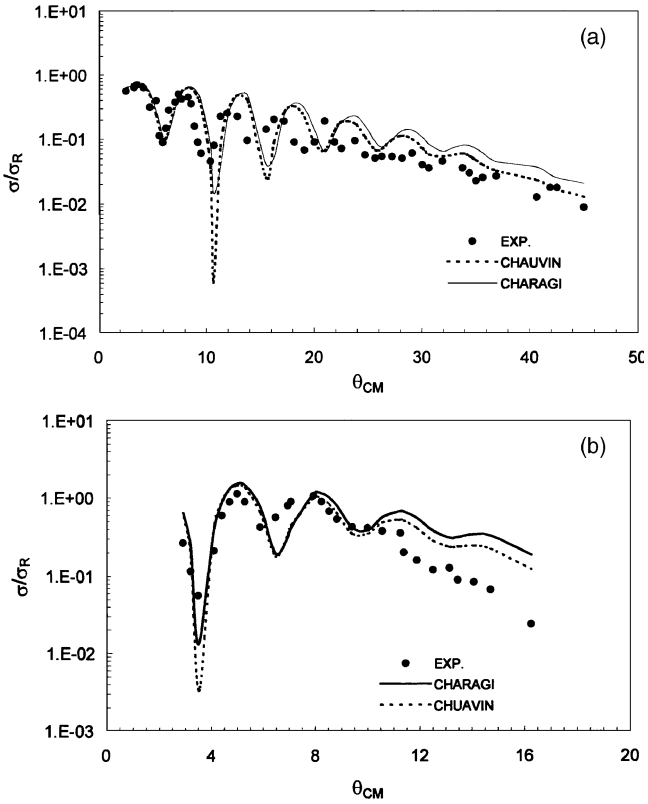


**Fig. 1.** a) Comparison between the use of Chauvin's nuclear-density parameters and the use of Charagi's parameters in the calculations of $\sigma/\sigma_{\rm R}$ for $^{12}$C-$^{12}$C at 300 MeV (zero range and $\beta = 0$). b) The same as a) but for $^{12}$C-$^{12}$C at 1016 MeV.

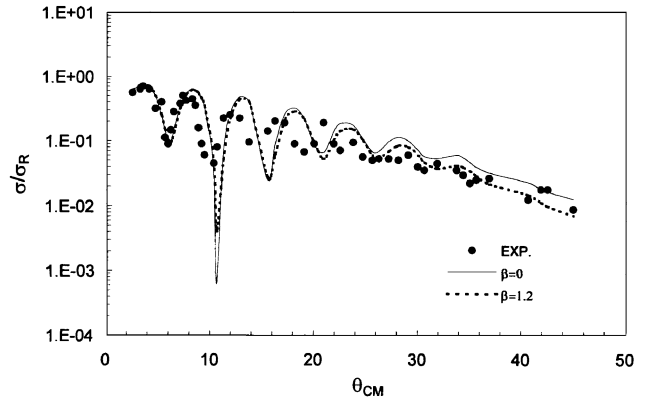


**Fig. 2.** The ratio of the calculated angular distribution to the Rutherford theoretical cross-sections ($\sigma/\sigma_{\rm R}$) displayed as a function of the C.M. scattering angle for $^{12}$C-$^{12}$C at 300 MeV (zero range).

parameter $\beta$ is adjusted to fit the experimental data. The chi-square test defined by

$$\chi^2 = \frac{1}{N}\sum_{i=1}^{N}\left(\frac{\sigma_i^{\rm theor.} - \sigma_i^{\rm exp}}{\Delta\sigma_i^{\rm exp}}\right)^2, \qquad (24)$$

is calculated for each incident energy and the density-dependent calculations have been done for the minimum

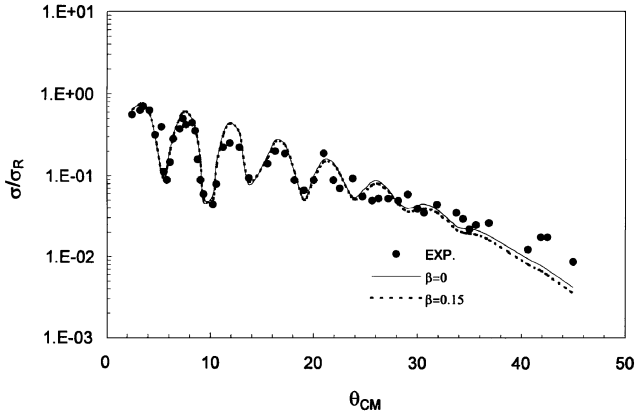


**Fig. 3.** The same as fig. 2 but for finite-range calculations.

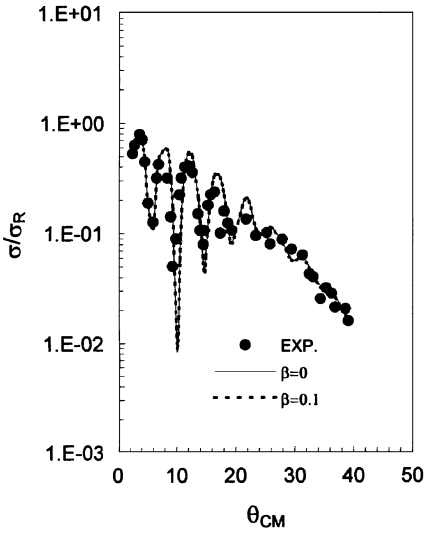


**Fig. 4.** The same as fig. 2 but for $^{12}$C-$^{12}$C at 360 MeV.

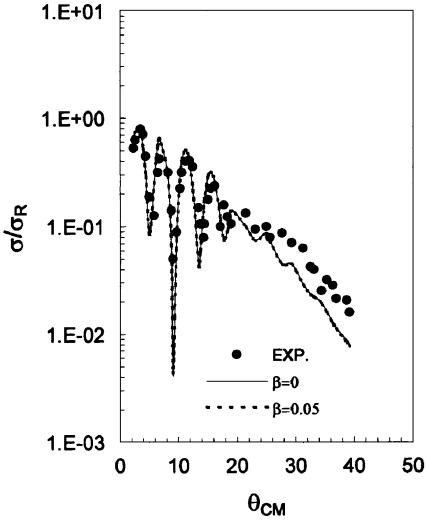


**Fig. 5.** The same as fig. 4 but for finite-range calculations.

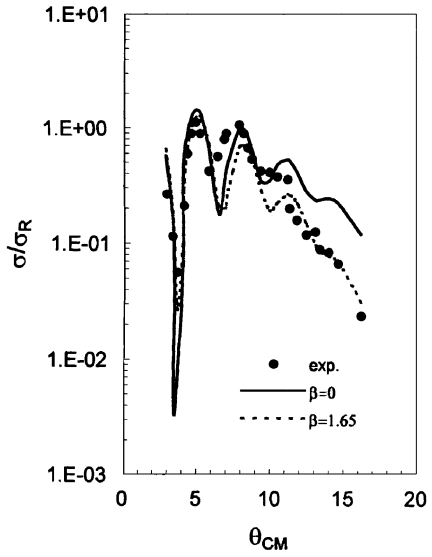


**Fig. 6.** The same as fig. 2 but for $^{12}$C-$^{12}$C at 1016 MeV.

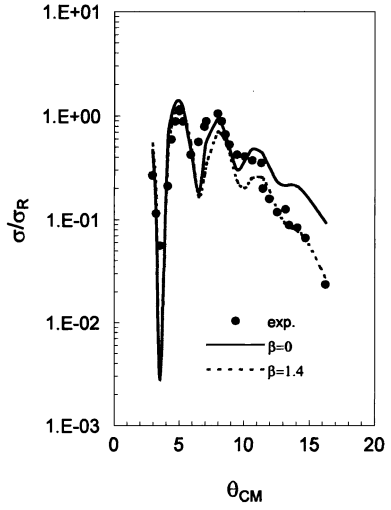


**Fig. 7.** The same as fig. 6 but for finite-range calculations.

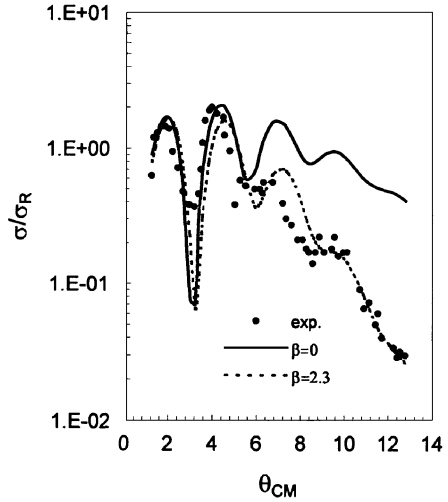


**Fig. 8.** The same as fig. 2 but for $^{12}$C-$^{12}$C at 1441 MeV (zero range).

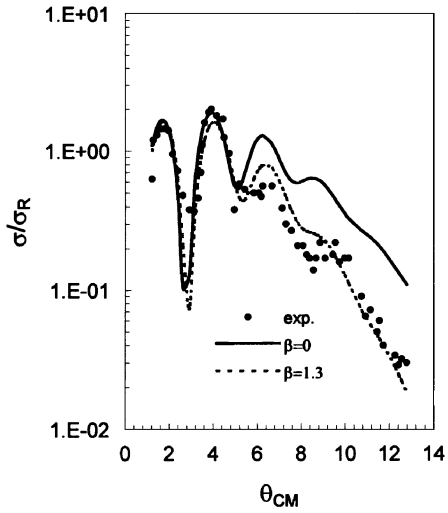


**Fig. 9.** The same as fig. 8 but for finite-range calculations.

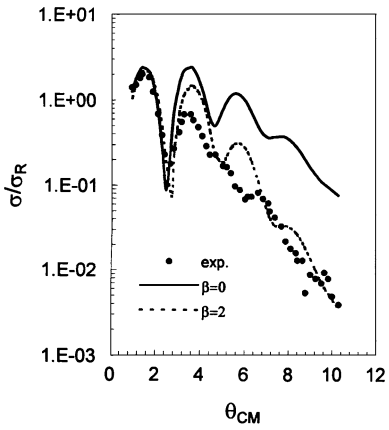


**Fig. 10.** The same as fig. 2 but for $^{12}$C-$^{12}$C 2400 MeV (zero range).

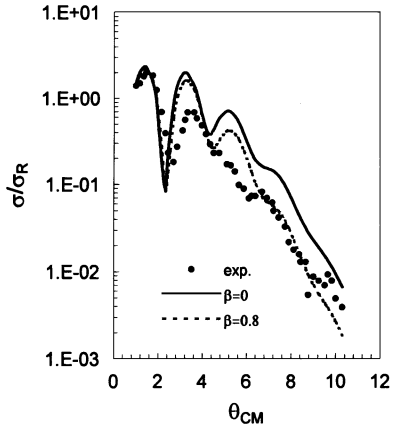


**Fig. 11.** The same as fig. 10 but for finite-range calculations.

value of $(\chi^2/N)$, that determines the best value of the density-dependent parameter $\beta$. Using these values of $\beta$, the total-reaction cross-section $\sigma_{\rm r}$ (for each incident energy) is also calculated and compared with either the experimental value or with that obtained from optical-model analysis given by others [2,25] or both. The results are tabulated in table 2.

**Table 2.** The parameters of the $^{12}$C-$^{12}$C heavy-ion system. The values of the range parameter "$r_0$" and that of "$\alpha_{\rm NN}$" are taken from ref. [26]. The experimental value of "$\sigma_{\rm r}$" are taken from ref. [25] while those given in the ordinary brackets are taken from refs. [2,25]. "$\beta$" is the density-dependent parameter. $R_{1/2}$ is the strong-absorption radius calculated from figs. 12-15.

| $E_{\rm lab}$ (MeV) | $r_0$ [26] (fm) | $\alpha_{\rm NN}$ [26] | $\beta$ (fm$^3$) | $\chi^2/N$ | $\sigma_{\rm r}$(exp.) (mb) | $\sigma_{\rm r}$(calc.) (mb) | $R_{1/2}$ (fm) |
|---|---|---|---|---|---|---|---|
| | 0.0 | | 0.0 | 2.99 | (1300)[a] | 1182 | 6.05 |
| 300 | | 0.85 | 1.2 | 2.76 | [2] | 1169 | 6.00 |
| | 1.285 | | 0.0 | 0.30 | | 1403 | 6.58 |
| | | | 0.15 | 0.27 | | 1397 | 6.50 |
| | 0.0 | | 0.0 | 0.84 | $1315 \pm 40$ | 1151 | 5.95 |
| 360 | | 0.87 | 0.1 | 0.84 | (1260)[a] | 1150 | 5.90 |
| | 1.171 | | 0.0 | 0.504 | [2] | 1328 | 6.37 |
| | | | 0.05 | 0.500 | | 1327 | 6.33 |
| | 0.0 | | 0.0 | 5.39 | $960 \pm 25$ | 938 | 5.46 |
| 1016 | | 1.0 | 1.65 | 0.94 | (1000)[a] | 905 | 5.37 |
| | 0.697 | | 0.0 | 3.31 | [2] | 985 | 5.60 |
| | | | 1.4 | 0.76 | | 953 | 5.48 |
| | 0.0 | | 0.0 | 44.34 | $907 \pm 50$ | 869 | 5.22 |
| 1441 | | 1.245 | 2.3 | 0.57 | (907)[a] | 812 | 5.05 |
| | 1.516 | | 0.0 | 5.33 | [25] | 1060 | 5.74 |
| | | | 1.3 | 0.21 | | 1008 | 5.60 |
| | 0.0 | | 0.0 | 245.3 | $864 \pm 45$ | 804 | 4.98 |
| 2400 | | 0.93 | 2.0 | 2.22 | $(806 \pm 30)$[a] | 749 | 4.80 |
| | 1.575 | | 0.0 | 8.57 | [25] | 986 | 5.49 |
| | | | 0.8 | 2.11 | | 952 | 5.38 |

[a] The values of $\sigma_{\rm r}$ (exp.) that are given in ordinary brackets are obtained from O.M. analysis.

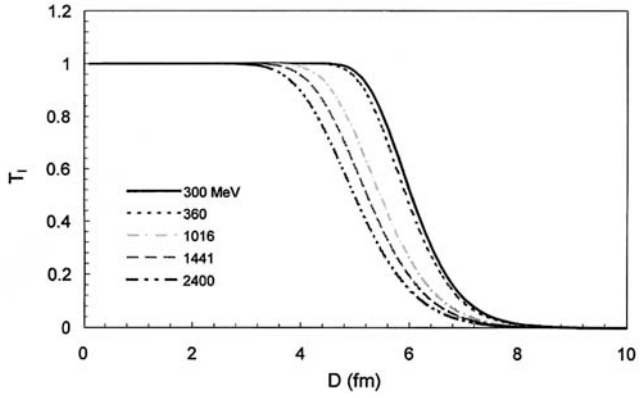


**Fig. 12.** Transparency as a function of the distance of closest approach assuming the classical Coulomb trajectory for $^{12}$C-$^{12}$C at different incident energies with zero range without in-medium effects ($\beta = 0$).

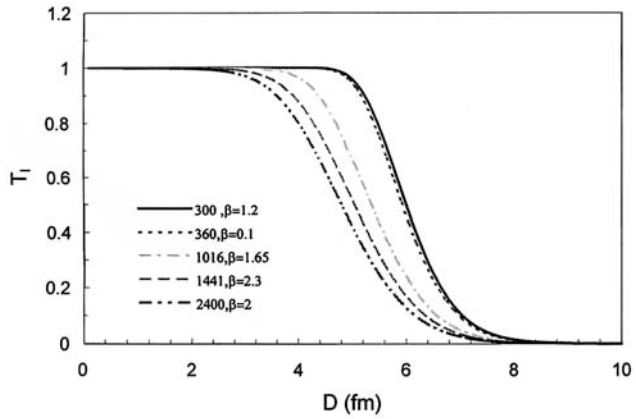


**Fig. 13.** The same as fig. 12 but with in-medium effects.

The transmission function ($T_l = 1 - |S_l|^2$) [25], is also calculated and displayed in figs. 12-15 as a function of the distance of closest approach, assuming the classical Coulomb trajectory defined by eq. (20). From these figures, the strong-absorption radius $R_{1/2}$is deduced for each incident energy and each corresponding value of $\beta$. The results are also listed in table 2. Figures 16, 17 below also show the behavior of the calculated $\sigma_{\rm r}(E_{\rm lab})$ as a function of the incident energy compared with the experimental data. All the above-mentioned calculations have been carried out using both the zero range and finite range with the NN range function of Gaussian type given by eq. (8). The values of the range parameter $r_0$ are listed in table 2 [26].

### 3.1 Elastic scattering

For $^{12}$C-$^{12}$C at 300 MeV (zero range), fig. 2 shows that calculation of $\sigma/\sigma_{\rm R}$ for $\beta = 1.2$ fm$^3$ ($\chi^2/N = 2.7$) gives a better fit to the experimental data than that with $\beta = 0$

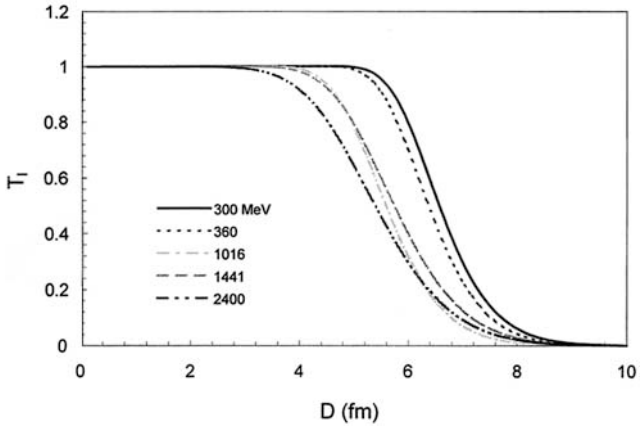


**Fig. 14.** The same as fig. 12 but for finite range ($\beta = 0$).

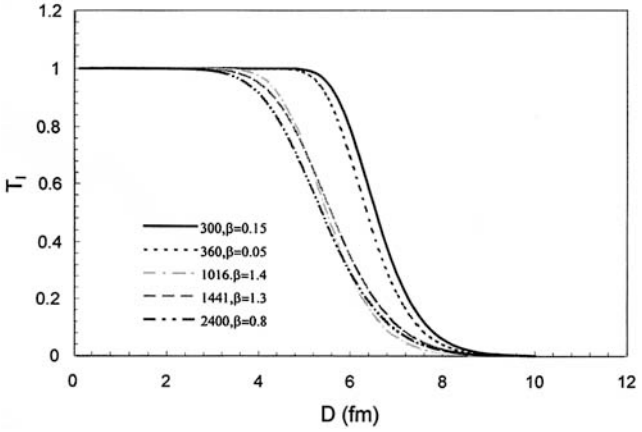


**Fig. 15.** The same as fig. 13 but for finite range.

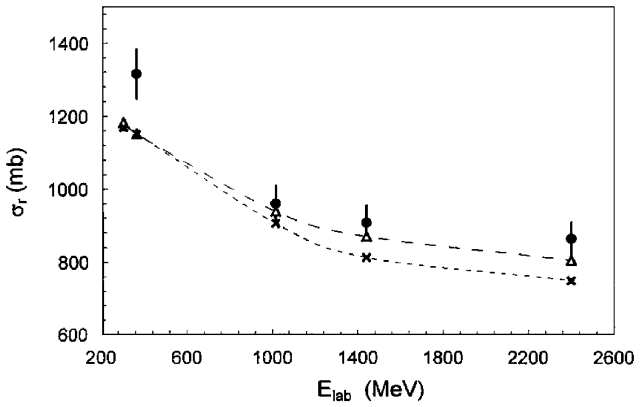


**Fig. 16.** Reaction cross-section of $^{12}$C-$^{12}$C (zero range). Triangles represent calculations without in-medium effects; crosses with in-medium effects and black circles with bars are the experimental data [2,25].

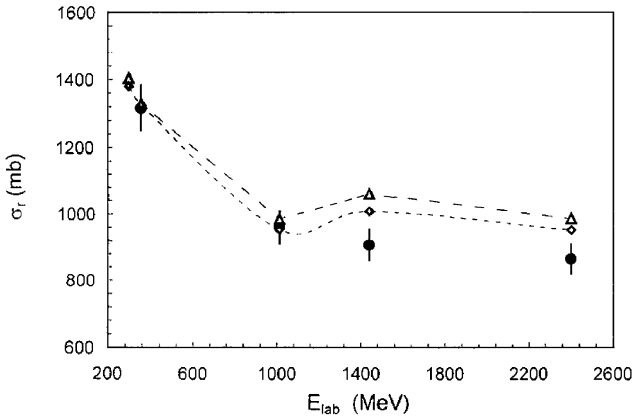


**Fig. 17.** The same as fig. 16 but for finite-range calculations but the calculations without in-medium effects are represented by diamonds.

($\chi^2/N = 2.9$). As for the finite range, fig. 3 shows the calculation of $\sigma/\sigma_{\rm R}$ for $\beta = 0$ ($\chi^2/N = 0.3$) and for $\beta = 0.15$ fm$^3$ ($\chi^2/N = 0.27$). There is no appreciable effect due to the use of medium effect in this case as can be seen from this figure.

At 360 MeV, the zero-range calculation of $\sigma/\sigma_{\rm R}$ for $\beta = 0$, ($\chi^2/N = 0.84$) is in good agreement with the experimental data as shown in fig. 4, and for this energy there is no need to use the density dependence. As for finite range, calculation either with $\beta = 0$ or $\beta = 0.05$ fm$^3$ does not improve the results of $\sigma/\sigma_{\rm R}$ in comparison with the experimental data as shown in fig. 5.

At 1016 MeV (zero range), fig. 6 shows that the introduction of the medium effects improves the results of the angular distribution of the elastic-scattering cross-section ($\sigma/\sigma_{\rm R}$) for $\beta = 1.65$ fm$^3$ in comparison with the experimental data. As for the finite-range calculations (fig. 7) the result of $\sigma/\sigma_{\rm R}$ with $\beta = 1.4$ fm$^3$ is better than that with $\beta = 0$ compared with the experimental data.

The zero-range calculation at 1441 MeV with density dependence ($\beta = 2.3$ fm$^3$) leads to an improvement of $\sigma/\sigma_{\rm R}$, especially at large scattering angles, compared with the experimental data as could be seen from fig. 8. As for the finite-range calculation, a better fit of $\sigma/\sigma_{\rm R}$ with $\beta = 1.3$ fm$^3$ than that with $\beta = 0$ is obtained in comparison with the experimental data as shown in fig. 9. Here, one notices that the calculations with finite range weaken the medium effects when the density-dependent parameter $\beta$ is less by 1 fm$^3$ than those with zero range.

The zero-range calculation of $\sigma/\sigma_{\rm R}$ at 2400 MeV with $\beta = 2$ fm$^3$ gives a better fit to the experimental data than that with $\beta = 0$, especially at large scattering angles, as shown in fig. 10. For finite range, the calculation of $\sigma/\sigma_{\rm R}$ is improved by introducing the medium effects ($\beta = 0.8$ fm$^3$) and a good fit to the experimental data is obtained as shown in fig. 11.

In general, the values of $\chi^2$ for elastic scattering does not show appreciable change for $E_{\rm lab} = 300$ and 360 MeV with introducing "$\beta$". However, a noticeable change is found for $E_{\rm lab} \geqslant 1016$ MeV with introducing in-medium effect.

### 3.2 Energy dependence of the absorption

Figures 12-15 show the distribution of the transmission coefficient, $T_l$ as a function of the internuclear distance of

closest approach assuming the classical Coulomb trajectory; $D$ associated with the partial-wave angular momentum $l$. $T_l$ must be considered as a qualitative picture of absorption of the reactions considered. The $T_l$ distribution can be used to define the strong-absorption radius $R_{1/2}$, a quantity that characterizes the system with respect to the strong absorption. $R_{1/2}$ is the distance of closest approach of the Coulomb trajectory associated with the partial wave $l_{1/2}$ for which $T_l = 1/2$; *i.e.* the distance where the incident particle has the same probability to be absorbed as to be reflected. For internuclear distances smaller than $R_{1/2}$ the absorption dominates, whereas for values larger than $R_{1/2}$ partial waves are mostly reflected in the elastic channel [25]. From these figures, the strong-absorption radius $R_{1/2}$ is deduced and the obtained values are listed in table 2. It could be seen that the transmission coefficient decreases as the incident energy increases. Accordingly, $R_{1/2}$ decreases with increasing incident energy as can be seen from the figures as well as from table 2. This weakening of absorption allows the colliding nuclei to interpenetrate deeper without being absorbed [25]. The effect of introducing the density dependence is to decrease the transmission coefficient and hence $R_{1/2}$ as is shown in the figures and table 2, which agrees with the fact that only the surface partial waves contribute nontrivially to the nuclear scattering [22].

### 3.3 Reaction cross-section

The calculated values of $\sigma_{\rm r}$ for each incident energy and the corresponding value of the density-dependent parameter $\beta$ as well as the experimental values [2,25] are listed in table 2. In this table the values of $\sigma_{\rm r}$ between brackets are obtained from the optical-model analysis [2,25]. From this table we notice that the calculated values of $\sigma_{\rm r}$ are less for $\beta \neq 0$ than those with $\beta = 0$. This means that medium effects lead to decreasing $\sigma_{\rm r}$ values.

For $^{12}$C-$^{12}$C at 300 MeV, although in case of finite-range calculations with medium effect of the elastic scattering $\sigma_{\rm r}$ has no appreciable change, the reaction cross-section is slightly improved (1397 mb) in comparison with that obtained by optical-model analysis (1300 mb) [2].

The calculated values of the reaction cross-section $\sigma_{\rm r}$ at 360 MeV with zero range either with $\beta = 0$ or $\beta = 0.1$ fm$^3$ are smaller than the experimental value ($1315 \pm 40$ mb). The finite-range calculations lead to closer values (1328 mb for $\beta = 0$ and 1327 mb for $\beta = 0.05$ fm$^3$) with the experimental one.

For zero-range calculations, the obtained value of $\sigma_{\rm r}$ at 1016 MeV with $\beta = 0$ (938 mb) is better than that with $\beta = 1.65$ fm$^3$ (905 mb) in comparison with the experimental value ($960 \pm 25$ mb). As for finite range, the calculated values of $\sigma_{\rm r}$ with either $\beta = 0$ or $\beta = 1.4$ fm$^3$ are in the range of the experimental value. The effect of introducing the density dependence stands for decreasing the value of $\sigma_{\rm r}$, but still within the range of the experimental value as could be seen from table 2.

At 1441 MeV and 2400 MeV, although the zero-range calculations of the reaction cross-section $\sigma_{\rm r}$ are less than the experimental value, the finite-range calculations exceed the experimental value as could be seen in table 2.

The general behavior of $\sigma_{\rm r}$ ($E_{\rm lab}$) is governed by the total NN cross-section $\bar{\sigma}_{\rm NN}$ through the covered energy range. This could be seen from figs. 16-17 for zero-range and finite-range calculations either with or without medium effects compared with the experimental values. Also, these figures show that although the calculated values of $\sigma_{\rm r}$ is either lower or greater than the experimental values, they exhibit the same behavior as a function of the incident energy.

## 4 Conclusion

The Pauli-blocking and Fermi-motion effects play an important role in the nucleus-nucleus elastic scattering. The simple version that treats these medium effects of the density-dependent total NN cross-section adopted in this work shows that the calculations are sensitive to the value of the density-dependent parameter $\beta$. It plays an important role in improving the elastic-scattering cross-section, $\sigma/\sigma_{\rm R}$, especially for energies greater than 30 MeV/A for the considered reaction. Although the obtained values of the reaction cross-section "$\sigma_{\rm r}$" are reduced as the overlap of the two nuclear densities is larger, *i.e.* for smaller internuclear distances, $\sigma_{\rm r}(E_{\rm lab})$ still exhibits the same behavior, as a function of the incident energy, as the experimental data. Generally, the value of the parameter $\beta$ for finite-range calculations is smaller than that of zero-range calculations. This means that finite-range calculations weaken the dependence on the in-medium effect.

This simple approach should be tested for other reactions such as $^{16}$O-$^{12}$C,$^{16}$O-$^{24}$Si,..., etc. for different incident energies and this is what we intend to do.

## References


1. R.G. Glauber, *Lectures on Theoretical Physics*, Vol. **I** (Interscience, New York, 1959).
2. J. Chauvin, A. Lounis, M. Buenerd, Phys. Rev. C **28**, 1970 (1983).
3. J. Chauvin, A. Lounis, M. Buenerd, J. Phys. G **11**, 262 (1985).
4. A. Vitturi, F. Zardi, Phys. Rev. C **36**, 1404 (1987).
5. S.M. Lenzi, A. Vitturi, F. Zardi, Phys. Rev. C **38**, 2086 (1988).
6. S.K. Charagi, S.K. Gupta, Phys. Rev. C **41**, 1610 (1990).
7. S.M. Lenzi, A. Vitturi, F. Zardi, Phys. Rev. C **40**, 2114 (1989).
8. M.K. Hegab, M.T. Hussein, N.M. Hassan, Z. Phys. A **336**, 345 (1990).
9. J. Feng, W.Q. Shen, Y.G. Ma, Z.Y. Zhu, Phys. Lett. B **305**, 9 (1993); W.Q. Shen *et al.*, Nucl. Phys. A **491**, 130 (1989).
10. Eiji I. Tanaka, Hisashi Horiuichi, Phys. Rev. C **54**, 3170 (1996).
11. D.A. Saloner, C. Toepffer, Nucl. Phys. A **283**, 8 (1977); D.A. Saloner, C. Toepffer, B. Fink, Nucl. Phys. A **283**, 131 (1977); N.J. Di Giacomo *et al.*, Phys. Lett. B **101**, 383 (1981).

12. G.Q. Li, R. Machleidt, Phys. Rev. C **48**, 1702 (1993).
13. G.Q. Li, R. Machleidt, Phys. Rev. C **49**, 566 (1994).
14. D. Klakow, G. Welke, W. Bauer, Phys. Rev. C **48**, 1982 (1993).
15. B.T. Haar, R. Malfliet, Phys. Rev. C **50**, 31 (1994).
16. Cai Xiangzhou *et al.*, Phys. Rev. C **58**, 572 (1998).
17. A.Sh. Ghazal, Arab J. Nucl. Sci. Appl. **35**, 159 (2002).
18. M.S.M. Nour El-Din, to be published in Egypt. J. Phys. (2004).
19. V.K. Lukyanov, B. Stowinski, E.V. Zemlyanaya, Phys. At. Nucl. **64**, 1273 (2001).
20. Jurgen Schaffner-Bielich, J. Phys. G. **27**, 337 (2001) and references therein.
21. C.A. Bertulani, J. Phys. G. **27**, L67 (2001).
22. S.K. Charagi, S.K. Gupta, Phys. Rev. C **46**, 1982 (1992).
23. A.Y. Abul-Magd, M. Talib Ali-Alhiai, Nuovo Cimento A **110**, 1281 (1997).
24. R. Hofstadter, *Nuclear and Nucleon Structure* (Benjamin, New York, 1963).
25. J.Y. Hostachy *et al.*, Nucl. Phys. A **490**, 441 (1988); M. Buenerd *et al.*, Nucl. Phys. A **424**, 313 (1984).
26. L. Ray, Phys. Rev. C **20**, 1857 (1979).